PHYSICAL REVIEW APPLIED **21,** 024050 (2024)

Magnetization-switching dynamics driven by chiral coupling

B.B. Vermeulen,[1,2,*] M. Gama Monteiro,[1] D. Giuliano,[1,2] B. Sorée,[1,3,4] S. Couet,[1]
K. Temst,[2,1] and V.D. Nguyen[1,†]

[1] *Interuniversity Microelectronics Center (IMEC), Kapeldreef 75, 3001 Leuven, Belgium*
[2] *Department of Physics and Astronomy, Quantum Solid-State Physics (QSP) Division, Katholieke Universiteit Leuven, Celestijnenlaan 200D Box 2414, 3001 Leuven, Belgium*
[3] *Department of Electrical Engineering, ESAT-INSYS Division, Katholieke Universiteit Leuven, Kasteelpark Arenberg 10, 3001 Leuven, Belgium*
[4] *Department of Physics, Universiteit Antwerpen, Groenenborgerlaan 171, 2020 Antwerp, Belgium*

(Received 18 August 2023; revised 20 January 2024; accepted 24 January 2024; published 26 February 2024)

The Dzyaloshinskii-Moriya interaction (DMI) is known to play a central role in stabilizing chiral spin textures such as skyrmions and domain walls (DWs). Electrical manipulation of DW and skyrmion motion offers possibilities for next-generation, scalable and energy-efficient spintronic devices. However, achieving the full potential of these nanoscale devices requires overcoming several challenges, including reliable electrical write and read techniques for these magnetic objects, and addressing pinning and Joule-heating concerns. Here, through micromagnetic simulations and analytical modeling, we show that DMI can directly induce magnetization switching of a nanomagnet with perpendicular magnetic anisotropy (PMA). We find that the switching is driven by the interplay between the DMI-induced magnetic frustration and the PMA. By introducing magnetic tunnel junctions to electrically access and control the magnetization direction of the PMA nanomagnet, we first show the potential of this concept to enable high-density field-free spin-orbit torque magnetic random-access memory. Ultimately, we demonstrate that it offers a way of transferring and processing spin information for logic operation without relying on current-driven DW or skyrmion motion.

DOI: 10.1103/PhysRevApplied.21.024050

I. INTRODUCTION

The Dzyaloshinskii-Moriya interaction (DMI) is an antisymmetric exchange interaction arising from spin-orbit coupling in magnetic systems with inversion-symmetry breaking [1–4]. The DMI Hamiltonian $\mathcal{H}_{\mathrm{DMI}} = -\mathbf{D}_{ij} \cdot \left(\mathbf{S}_i \times \mathbf{S}_j\right)$ favors orthogonal alignment of neighboring magnetic moments $\mathbf{S}_i$ and $\mathbf{S}_j$ with a fixed chirality (or handedness) given by the DMI vector $\mathbf{D}_{ij}$. DMI is being actively researched to form noncollinear spin textures such as chiral domain walls (DWs) [5,6] and skyrmions [7] within ferromagnet–heavy-metal bilayer systems [8,9]. The electrical manipulation of these magnetic objects at the nanoscale holds great promise for next-generation spintronic devices [10,11].

Recently, Luo *et al.* [12] experimentally demonstrated that DMI can generate chiral coupling between adjacent out-of-plane (OOP) and in-plane (IP) magnetic regions. Unlike coupling in vertically stacked systems [13,14], this lateral coupling has enabled the creation of artificial spin-ice [15] and skyrmion structures. This discovery led to the demonstration of current-driven DW logic gates [16]. Very recently, Yu *et al.* [17] theoretically revealed that manipulating the strength of the DMI via a gate voltage can lead to magnetization switching by skyrmion expansion. Nevertheless, achieving the complete potential of these devices requires overcoming challenges related to the electrical manipulation of DWs and skyrmions at the nanoscale, involving reliable write and read techniques and addressing issues of pinning and Joule heating.

Here, through micromagnetic simulations and analytical modeling, we demonstrate that chiral coupling induced by DMI can be exploited as a direct mechanism to switch a nanomagnet with perpendicular magnetic anisotropy (PMA). The working principle of magnetization switching induced by chiral coupling is described in Fig. 1(a). Initially, the interfacial DMI generates chiral coupling between the left OOP region pointing up (“↑”), the IP region pointing left (“←”), and the right OOP region pointing down (“↓”), by favoring a unique rotation direction of the magnetization, depending on the sign of the DMI [12]. In this concept, the switching of the left OOP

---

[*] bob.vermeulen@imec.be
[†] van.dai.nguyen@imec.be

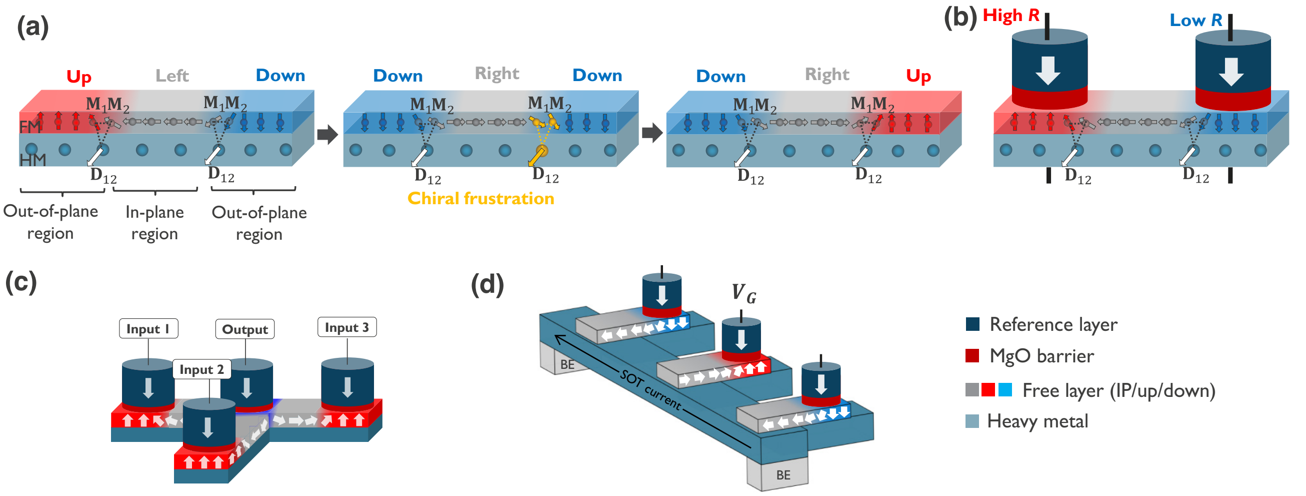

FIG. 1. (a) Concept of magnetization switching driven by chiral coupling, where two OOP regions separated by an IP region are initially coupled in the ↑←↓ configuration due to the DMI induced by the heavy-metal (HM)–ferromagnet (FM) interface. The switching of the left OOP region leads to a magnetic frustration due to the chiral coupling. This frustration is the driving force to switch the right OOP region to the ↑ direction. (b) By electrically accessing the OOP regions with MTJs (made of a reference layer, an MgO tunneling barrier, and a free layer), this concept leads to direct antiparallel coupling of adjacent MTJs. (c) By the coupling of one MTJ with three other MTJs, a compact minority gate is obtained, containing both NAND and NOR logic operations in a single logic gate. (d) By inducing the switching of the IP region by SOT and controlling the switching of the MTJs by gate voltage, this concept leads to a compact field-free SOT-MRAM solution. BE, bottom electrode.

region from ↑ to ↓ leads to a chiral frustration since the new configuration does not have the chirality favored by DMI (chiral frustration refers to the high-energy state that does not minimize the DMI energy). We show that the energy of this frustrated state E_{frust} is the driving force to overcome the energy barrier E_b for switching the right OOP region from ↓ to ↑, such that the configuration has the chirality favored by DMI. Chiral coupling, therefore, provides an alternative to induce magnetization switching, unlike present methods, including spin-transfer torque (STT) [18,19], spin-orbit torque (SOT) [20,21], voltage-controlled magnetic anisotropy (VCMA) [22], and optical techniques [23,24].

By leveraging magnetic-tunnel-junction (MTJ) technology to electrically access the magnetization of the OOP regions [see Fig. 1(b)], we present an unconventional approach for dynamically controlling an MTJ through switching induced by chiral coupling. This approach allows the direct coupling of two adjacent MTJs in antiparallel directions, enabling logic operation during the electrical write and read operations of MTJs. Significantly, this represents a pioneering method to propagate spin information without relying on conventional current-driven DW or skyrmion motion [Fig. 1(b)]. Finally, we demonstrate the technological promise of this concept by enabling compact spin logic gates [Fig. 1(c)] and the realization of high-density and field-free SOT magnetic random-access memory (MRAM) [Fig. 1(d)].

II. METHODS

Micromagnetic simulations are performed with MuMax3 [25], with magnetic thickness $t_{\text{mag}} = 1.6$ nm, $1 \times 1 \times 1.6\ \text{nm}^3$ discretization, and the following magnetic parameters: saturation magnetization $M_s = 800$ kA/m, exchange constant $A = 20$ pJ/m, and damping constant $\alpha = 0.05$. The anisotropy constant K_u in the OOP region and the DMI constant D are variables and are specified in the text. $K_u = 0\ \text{kJ/m}^3$ in the IP region. The Landau-Lifshitz-Gilbert (LLG) equation is solved:

$$\dot{\mathbf{m}} = -\mu_0\gamma\mathbf{m} \times \mathbf{H}_{\text{eff}} + \alpha\mathbf{m} \times \dot{\mathbf{m}} + \boldsymbol{\tau}_{\text{SOT/STT}}, \qquad (1)$$

where $\mathbf{m}$, μ_0, γ, $\mathbf{H}_{\text{eff}}$, α, and $\boldsymbol{\tau}_{\text{SOT/STT}}$ are the unit magnetization vector, the vacuum magnetic permeability, the gyromagnetic ratio, the effective field, the Gilbert damping constant, and the applied SOT or STT. We always initialize and relax the system by solving the LLG equation with no precessional term, therefore pointing the magnetization towards the nearest energy minimum. We then study the system dynamics when magnetization rotation is imposed or SOT or STT is applied by solving the full LLG equation.

SOT (with an in-plane current) is implemented as a Slonczewski-like torque:

$$\boldsymbol{\tau}_{\text{SOT}} = -\frac{\gamma|\theta_{\text{SH}}|J\hbar}{2eM_s t_{\text{mag}}}\left(\mathbf{m} \times \mathbf{m} \times \mathbf{p} + \xi_{\text{SOT}}\mathbf{m} \times \mathbf{p}\right), \qquad (2)$$

where $\theta_{\mathrm{SH}} = 0.12$ is the spin Hall angle, J is the current density, $\hbar$ is the reduced Planck constant, e is the electron charge, $\xi_{\mathrm{SOT}} = 0.22$ is the fieldlike-to-dampinglike SOT ratio, and $\mathbf{p}$ is the unit spin polarization vector. In MuMax3, we adapt Eq. (2) using the default STT implementation with the following parameter set: $P_{\mathrm{mumax}} = |\theta_{\mathrm{SH}}|$, $\Lambda = 1$, $\epsilon' = |\theta_{\mathrm{SH}}|\xi_{\mathrm{SOT}}/2$, $\mathbf{p} = \mathrm{sgn}(\theta_{\mathrm{SH}})\mathbf{e}_J \times \mathbf{e}_z$, with $\mathbf{e}_J$ the direction of the SOT current, and $J_{z,\mathrm{mumax}} = J$.

STT (with a current along the z direction) is implemented as a Slonczewski-like torque:

$$\boldsymbol{\tau}_{\mathrm{STT}} = \frac{\gamma P J \hbar}{2eM_s t_{\mathrm{mag}}} (\mathbf{m} \times \mathbf{p} \times \mathbf{m}) , \tag{3}$$

where $P = 0.5$ is the spin polarization, J is the current density, and $\mathbf{p}$ is the fixed layer polarization vector. In MuMax3, we adapt Eq. (3) using the default STT implementation with the following parameter set: $P_{\mathrm{mumax}} = P$, $\Lambda = 1$, $\epsilon' = 0$, and $J_{z,\mathrm{mumax}} = J_z$ [26].

III. RESULTS AND DISCUSSION

A. Switching dynamics driven by chiral coupling

The system is made of square IP and OOP regions [see Fig. 2(a)]. After relaxation, a part of the IP region is switched to reach a high-energy frustrated state. We then find that the switching of the OOP region relies on the competition between E_{frust} and E_b, resulting mainly from the DMI strength, D, and the perpendicular anisotropy of the OOP region, K_u. The state of the OOP region is mapped out in Fig. 2(b) for a range of K_u and D values corresponding to typical experimental values [8]. The red and blue regions correspond to the switching and nonswitching states of the OOP region, respectively. The results reveal a general trend that increasing K_u leads to a higher energy barrier, requiring a higher DMI strength to switch the OOP region.

The red region in Fig. 2(b) corresponds to $E_{\mathrm{frust}} > E_b$ and the deterministic switching of the OOP region. For low DMI and low K_u ($D < 1$ mJ/m^2 and $K_u < 425$ kJ/m^3), the OOP region switches uniformly, i.e., coherent switching.

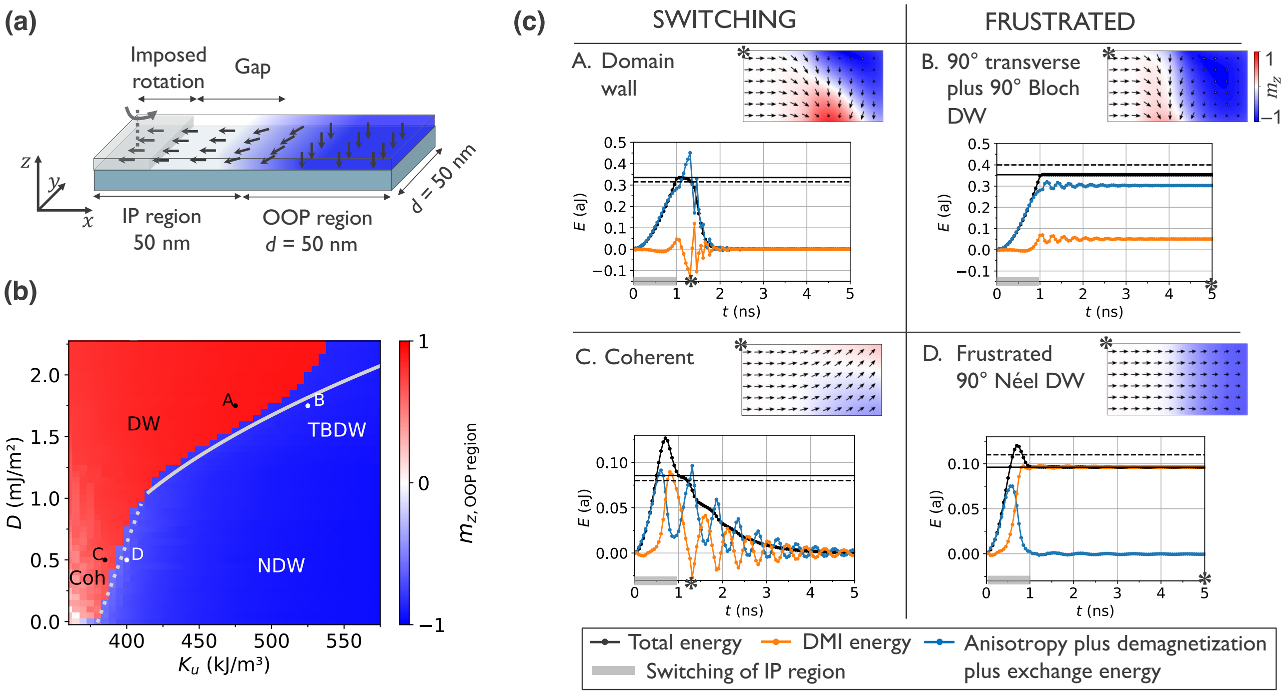

FIG. 2. (a) System studied for the magnetization switching dynamics of a PMA nanomagnet driven by chiral coupling, where a 20-nm part of the IP region is rotated uniformly from ← to → in 1 ns in steps of 1.8°, and the rest of the system is relaxed for 5 ns. (b) z component of the magnetization of the OOP region after imposition of the switching of the IP region, depending on K_u of the OOP region and on DMI, after relaxation for 5 ns. The red region corresponds to the working window where the OOP region switches by chiral coupling. The types of switching scheme and of frustrated state are indicated in the switching and nonswitching regions, respectively. The dotted and solid lines are for $D = (2/\pi)K_{\mathrm{eff}}d$ and $D = \sqrt{AK_{\mathrm{eff}}}$ approximating the working window. (c) Examples of different switching schemes and frustrated states: evolution of the micromagnetic energies (relative to the initial configuration) and micromagnetic configurations (top view) at the time indicated by an asterisk. The values of DMI and K_u correspond to points A, B, C, and D in (b). The solid and dashed lines are an indication of the energy of the frustrated state E_{frust} and the energy barrier E_b, respectively. In cases B and D, $E_{\mathrm{frust}} < E_b$ and the system remains in a high-energy state. In cases A and C, $E_{\mathrm{frust}} > E_b$ and the OOP region switches by chiral coupling. Coh, coherent.

For higher DMI and K_u, a DW nucleates and propagates to switch the OOP region, i.e., DW switching (see Videos 1 and 2 in Appendix A). We also found that OOP regions larger or smaller than 50 nm have DW- or coherent-dominated switching schemes, respectively. These results show that the switching process induced by chiral coupling is similar to field- or current-driven switching schemes [26,27]. Interestingly, when $E_{\text{frust}} < E_b$ (i.e., the blue region) and the OOP region does not switch (despite the IP region being held in the → direction), the system is found to remain in a frustrated state with high DMI energy. A frustrated 90° Néel DW (NDW) is formed in the low-DMI case (below $1.25\ \text{mJ/m}^2$), while a complex state combining a 90° transverse DW and a 90° Bloch DW (TBDW) is formed in the high-DMI case [see insets *B* and *D* in Fig. 2(c)].

The evolution of the energies for the different switching behaviors and frustrated states is shown in Fig. 2(c).

For low DMI (below $1\ \text{mJ/m}^2$), in the frustrated NDW state [inset *D* in Fig. 2(c)], the system remains stuck in a high-DMI-energy state. When K_u is decreased [from inset *D* in Fig. 2(c) to inset *C* in Fig. 2(c)] to meet the switching condition $E_{\text{frust}} > E_b$, the OOP region switches coherently. During the switching, we observe a decrease of the DMI energy and an increase of the anisotropy energy, which corresponds to the energy barrier of the OOP region. The system then reaches the equilibrium configuration with damped oscillations.

For high DMI, in the frustrated TBDW state [inset *B* in Fig. 2(c)], the system is stuck in a high-DMI-energy and high-exchange-energy state. When K_u is decreased [from inset *B* in Fig. 2(c) to inset *A* in Fig. 2(c)], the OOP region switches by DW nucleation and propagation. An increase of the anisotropy and exchange energy and a decrease of the DMI energy are observed during the switching. This energy variation is attributed to the nucleation of a chiral DW to switch the OOP region, which has an average energy density of $4\sqrt{AK_{\text{eff}}} - \pi D$ [6,28], where A and K_{eff} are the exchange stiffness and the effective anisotropy, respectively. Moreover, an additional decrease of the DMI energy is observed due to the domain nucleation in the OOP region which is in the direction favored by DMI.

To establish the material parameters governing the switching process, we introduce an analytical model based on the switching criterion $E_{\text{frust}} > E_b$.

In the low DMI range in Fig. 2(b) (i.e., below $1\ \text{mJ/m}^2$), the switching condition between coherent switching and frustrated-NDW state is obtained with $E_{\text{frust}} = \pi D d$ [12] and $E_b = K_{\text{eff}} d^2 + (\pi/2) D d$, where d is the size of the OOP region. Applying $E_{\text{frust}} > E_b$, we obtain the following switching condition:

$$D > \frac{2}{\pi} K_{\text{eff}} d, \tag{4}$$

where $K_{\text{eff}} = K_u - K_{\text{sh1}}$, where K_{sh1} is the shape anisotropy in the OOP region. This is represented as a dashed line in Fig. 2(b) with $K_{\text{sh1}} = 380\ \text{kJ/m}^2$, providing good agreement with the simulation results.

The same criterion can be applied for DW switching and frustrated-TBDW state in the high DMI range in Fig. 2(b) (i.e., above $1\ \text{mJ/m}^2$). The energy barrier corresponds to the nucleation of a chiral DW of average energy density $4\sqrt{AK_{\text{eff}}} - \pi D$ and an additional decrease of the DMI energy due to the nucleated domain. Comparing the DMI-energy term (of the same order as D) with the exchange, anisotropy, and demagnetization energy (of the same order as $\sqrt{AK_{\text{eff}}}$), we obtain the following switching condition:

$$D > \sqrt{AK_{\text{eff}}}, \tag{5}$$

where $K_{\text{eff}} = K_u - K_{\text{sh2}}$, where K_{sh2} is the shape anisotropy for DW switching. K_{sh2} is taken as the value of K_u below which $m_{z,\text{OOP region}} = 0$ (for $D = 0\ \text{mJ/m}^2$), leading to $K_{\text{sh2}} = 360\ \text{kJ/m}^3$. This is represented as a solid curve in Fig. 2(b), again in good agreement with the simulation results.

Note that the transition between the different switching schemes and frustrated states is a gradual process. More information on those transitions and the switching time is available in Figs. 6 and 7 in Appendixes B and C, respectively. Finally, Fig. S1 in Supplemental Material [29] shows the scaling potential of this concept.

Our analytical model and our energy assessment of nontrivial magnetic configurations provide profound insights into the physics of DMI-induced magnetization switching in perpendicular nanomagnets. In the following, by introducing an electrical method to induce a frustrated state, we demonstrate an approach for developing high-density and field-free SOT-MRAM devices. Ultimately, we pioneer an efficient method for propagating spin information for logic operations.

B. Enabling high-density and field-free SOT MRAM

With its remarkable characteristics of high retention and fast switching, SOT MRAM with PMA MTJs is seen as the next evolution of MRAM technology [30]. Nevertheless, two key obstacles remain to be addressed: field-free switching and high storage density [31,32]. The first challenge is linked to the need for an external field for deterministic SOT switching in a PMA MTJ. Field-free SOT switching can be achieved in an IP MTJ [33], but its retention is limited. The second challenge results from the additional electrodes needed for the writing and reading paths, thereby increasing the footprint. To increase density, multiple MTJ devices sharing the same SOT track are being developed, where the selective writing operation is controlled by the VCMA effect [34]. Recently, this concept was experimentally demonstrated but an external field is still required [35].

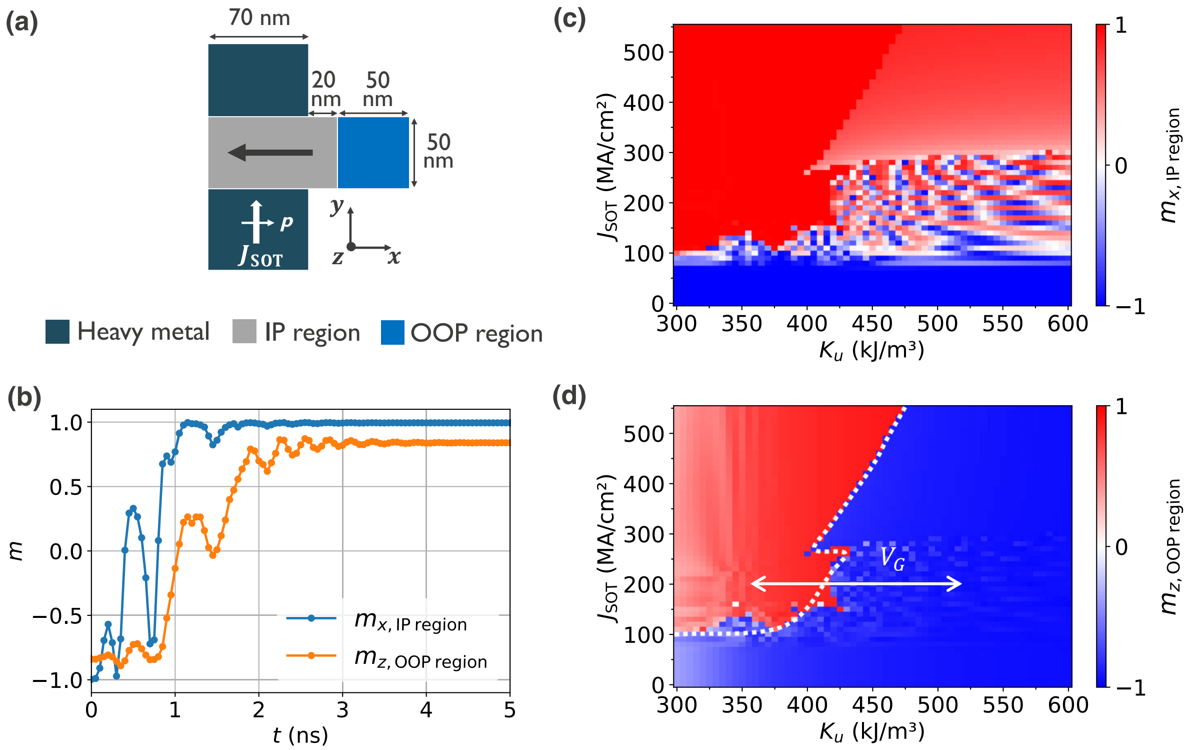

FIG. 3. (a) System studied for SOT switching of chirally coupled nanomagnets. (b) Evolution of the magnetization of the IP and OOP regions for $J_{\mathrm{SOT}} = 200$ MA/cm^2, $K_u = 400$ kJ/m^3, and $D = 1.5$ mJ/m^2. (c),(d) x and z components of the magnetization of the IP and OOP regions, respectively, after application of SOT on the IP region for 5 ns, depending on J_{SOT} and K_u, with $D = 1.5$ mJ/m^2. Red and blue correspond to the switching state and the nonswitching state, respectively, for (c) the IP region and (d) the OOP region. The dotted line is a guide to delimit the switching window. By controlling the PMA of the OOP region with a gate voltage V_G, we can control the switching of the OOP region.

Here we demonstrate that field-free SOT switching of the IP region in type-Y configuration (current in the y direction [33]) can subsequently induce the switching of the OOP region by chiral coupling. Therefore, this concept allows field-free SOT MRAM as well as high density using the multipillar configuration.

The system studied is represented in Fig. 3(a). Figure 3(b) shows an example of the switching of the OOP region after the switching of the IP region by SOT. Figures 3(c) and 3(d) show the switching state of the IP and OOP regions, respectively, as a function of the SOT current density J_{SOT} and K_u, using standard properties of the commonly used Pt/Co material (see Sec. II). Figure 3(c) reveals that a critical SOT current $J_{\mathrm{SOT},c} \approx 100$ MA/cm^2 (similar to experimental values [36]) is required to overcome the chiral coupling and to switch the IP region. Figure 3(d) shows that for $J_{\mathrm{SOT}} > J_{\mathrm{SOT},c}$, the OOP region switches for K_u below a certain threshold, where the SOT and the chiral coupling overcome the energy barrier of the OOP region. For J_{SOT} between 100 and 250 MA/cm^2, the IP region switches by increasing oscillations attributed to the competition between SOT current, chiral coupling, and the energy barrier of the OOP region (see Fig. 8 in Appendix D). If the OOP region switches, the IP region gets stabilized, otherwise the oscillatory behavior continues. For J_{SOT} above 250 MA/cm^2, the IP region switches in one step (see Fig. 8 in Appendix D). If the SOT is cut off and the OOP region remains unchanged, the IP region switches back to preserve the DMI chirality. More information on the SOT switching behaviors and switching time is available in Figs. 8 and 9 in Appendix D.

By accessing the OOP region with a PMA MTJ, this concept enables field-free SOT-MRAM devices. On the basis of the switching criterion $E_{\mathrm{frust}} > E_b$, the MTJ switches for K_u only below a certain threshold. Low K_u would, however, hinder the high retention target for MRAM application. Therefore, we propose the use of a gate voltage to selectively reduce the energy barrier of the OOP region by the VCMA effect during the write operation. For a realistic experimental value of the VCMA coefficient $\xi \approx 100$ fJ/Vm [22,37,38], with free-layer thickness $t_{\mathrm{FL}} = 1.6$ nm and tunneling-barrier thickness $t_{\mathrm{barrier}} = 1$ nm, an applied voltage of 1 V leads to a reduction $\Delta K_u \approx 160$ kJ/m^3, as illustrated in Fig. 3(d). Therefore, we propose implementing multipillar devices sharing the same SOT track to increase density as shown in

Fig. 1(d). For a given SOT current, the switching operation is electrically controlled by the selective application of a gate voltage V_G, leading to so-called V_G SOT MRAM. This drastically reduces the number of terminals that contribute to the large footprint found in traditional SOT-MRAM devices [35,39].

Moreover, by implementing the devices with separate layers for the SOT and the MTJ free-layer material (see Note 1 in Supplemental Material [29]), new high-efficiency SOT materials [40] can be integrated to reduce the switching currents without compromising the MTJ properties.

This proof of concept simultaneously addresses the low retention of IP MTJs and the external field needed with PMA-MTJ devices, providing a potential solution for field-free and high-density SOT MRAM.

It is worth noting that this device proposal also functions by application of SOT under both the IP region and the OOP region, where the field-free switching behavior is then attributed to the symmetry breaking induced by chiral coupling [12]. However, SOT current flowing underneath the MgO barrier in this configuration potentially poses reliability issues [41].

C. Processing spin information for logic operation

We now demonstrate that magnetization switching driven by chiral coupling offers an unconventional method to propagate and to process spin information. We show that introducing chiral coupling between adjacent MTJs enables one to build electrically controlled inverter and minority gates containing both NAND and NOR functionalities. Indeed, spintronic majority or minority gates are currently being explored as promising candidates to simplify logic circuits and to tackle dimensional scaling challenges [42,43]. Moreover, our device concept enables one to build compact logic gates without the need for current-driven DW or skyrmion motion, alleviating issues such as pinning and Joule heating (see Note 2 in Supplemental Material [29]). While concepts involving exchange or dipolar coupling also provide current-free information propagation, they come with challenges for practical spin logic applications. Those are linked to narrow operating windows and difficulties in implementing the required inverter operations for exchange coupling [44] and the requirement of an external clocking field as well as potential interference with the stray field of MTJs for dipolar coupling [45].

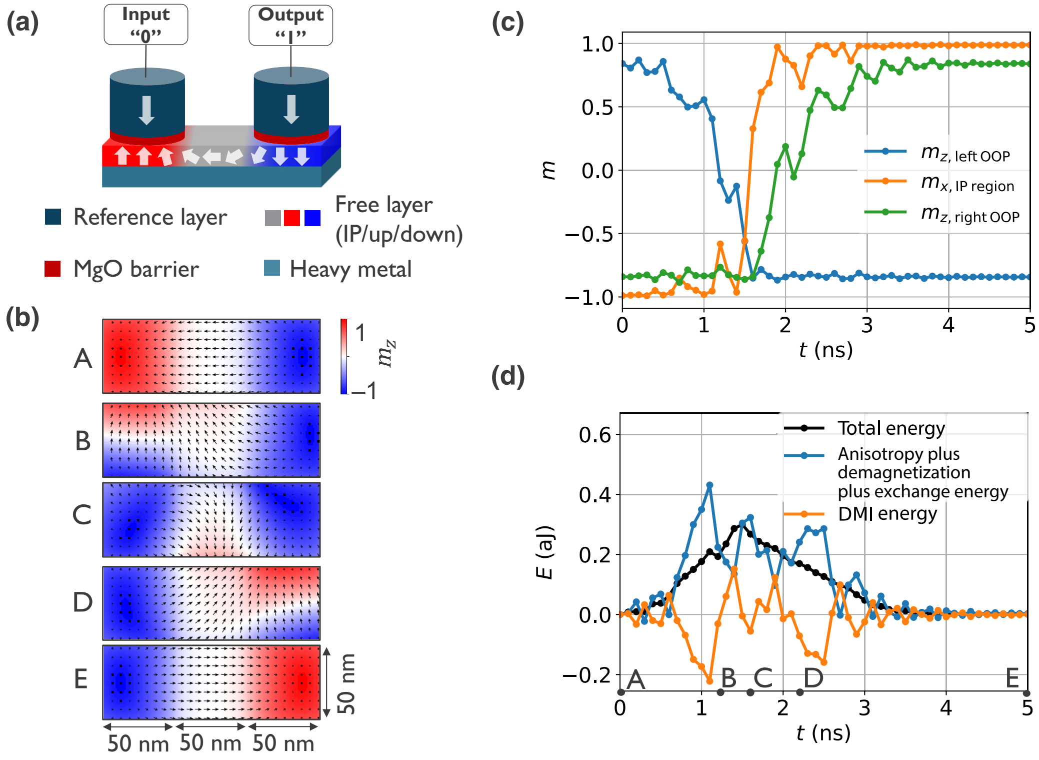

FIG. 4. (a) Chiral inverter made of two MTJs coupled in opposite directions by DMI via an interconnecting IP free layer. (b) Micromagnetic configuration (top view) during the switching of two chirally coupled MTJs. $K_u = 400$ kJ/m^3 in the OOP regions and $D = 1.5$ mJ/m^2 [i.e., inside the working window identified in Fig. 2(b)]. STT with current density $J_{\text{STT}} = 30$ MA/cm^2 is applied for 5 ns on the left MTJ. The switching of the left MTJ induces the switching of the IP region and in turn the switching of the right MTJ, due to chiral coupling. (c) Evolution of the magnetization of the left MTJ, the IP region, and the right MTJ. (d) Evolution of the micromagnetic energies. The time corresponding to cases A–E in (b) is indicated.

(a)

Input 1	Input 2	Input 3	Output
0	0	0	1
0	0	1	1
0	1	0	1
0	1	1	0
1	0	0	1
1	0	1	0
1	1	0	0
1	1	1	0

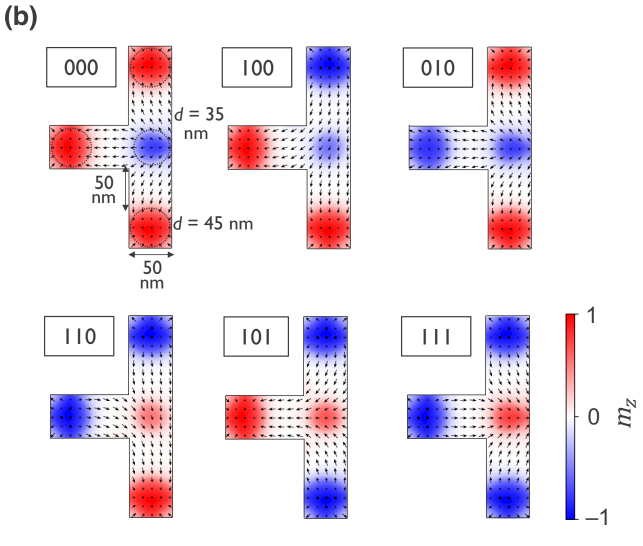

FIG. 5. (a) Truth table of a minority gate with three inputs, containing both the NAND and the NOR functionalities when one input is fixed to “0” or “1,” respectively. (b) Micromagnetic configuration (top view) of four chirally coupled MTJs forming a minority gate [see Fig. 1(c)], for all the possible logic inputs. $K_u = 600$ kJ/m^3 in the OOP regions and $D = 1$ mJ/m^2. The MTJs are indicated by circles formed by a dotted line with diameter d in the first image. Logic inputs “001” and “011” are not represented because they are equivalent to “100” and “110” by symmetry, respectively. The output switches when two or three inputs are switched by application of STT.

Figures 4(a) and 4(b) show a schematic and the operation of a chiral inverter (i.e., a logic NOT gate) formed by two chirally coupled PMA MTJs via an interconnecting IP free layer. In the initial state, the left MTJ is pointing up (“↑” i.e., input “0”), the IP region is pointing left (“←”), and the right MTJ is pointing down (“↓” i.e., output “1”), denoted as the ↑←↓ configuration (A). Then, the switching of the left MTJ by application of STT (B) induces the switching of the interconnecting IP region (C), due to both chiral coupling and STT precession. This, in turn, leads to the switching of the right MTJ due to chiral coupling (D) and the system settles in the ↓→↑ configuration (E) to satisfy the DMI chirality. In Figs. 4(c) and 4(d), we observe the sequential switching of the input MTJ, IP region, and output MTJ. After switching of the input MTJ, the system enters a high-energy frustrated state that enables the switching of the output MTJ. During the switching of the MTJs, we observe a decrease of the DMI energy, and an increase of the other energy terms, as in Fig. 2(c).

The chiral inverter is a basic element to build more-complex logic devices. By coupling one output MTJ with three input MTJs [see Fig. 1(c)], we can indeed construct a compact minority gate with the truth table shown in Fig. 5(a). For a certain configuration of the three inputs, the lowest energy state will be the one that minimizes the number of frustrated states. The magnetic state of the output MTJ will therefore follow the direction favored by the majority of inputs, as shown in Fig. 5(b). In the initial state, the three inputs are ↑ (“000”) and the output is ↓ (“1”). Switching one input (e.g., “100”) is not sufficient to switch the output since its state is dictated by the two other inputs. Switching two or three inputs (e.g., “101”) leads to the switching of the output to ↑ (“0”).

IV. CONCLUSION

In conclusion, we have reported the magnetization switching of a PMA nanomagnet induced by chiral coupling, where the switching process is controlled by the interplay between chiral frustration and the energy barrier of the nanomagnet. We found that the switching mechanisms correspond to coherent switching or DW switching depending on the DW width, as during conventional STT and SOT switching. The switching condition was found to depend on the balance between the chiral coupling and the energy barrier, resulting from the DMI strength and the PMA of the nanomagnet. We also demonstrated the technological potential of this concept by enabling field-free high-density SOT-MRAM devices as well as compact chiral-inverter and minority logic gates without relying on current-driven information propagation. A path towards the experimental realization of this device concept is presented in Supplemental Material [29], taking into account the availability of DMI materials [8] and the magnetically interconnected MTJs technology [46]. This concept will provide an unconventional avenue to explore the intriguing physics of DMI and magnetic frustration in device operation through electrical detection of MTJs.

ACKNOWLEDGMENTS

This work was performed as part of the imec IIAP core CMOS and Exploratory Logic Program of Intel Corporation. B.V. acknowledges FWO-Vlaanderen for a Strategic Basic Research PhD fellowship (No. 1S72223N). K.T. acknowledges Katholieke Universiteit Leuven (KUL) C1 Grant No. C14/18/074 and the FWO-FNRS Weave program.

APPENDIX A: COHERENT-SWITCHING AND DW-SWITCHING SCHEMES

Videos 1 and 2 show the coherent-switching and DW-switching schemes described in Fig. 2, where the IP region

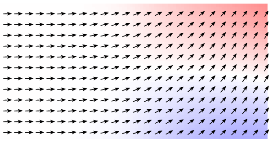

VIDEO 1. Coherent-switching scheme with $D = 0.5$ mJ/m^2 and $K_u = 385$ kJ/m^3.

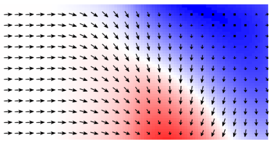

VIDEO 2. DW-switching scheme with $D = 1.75$ mJ/m^2 and $K_u = 475$ kJ/m^3.

is rotated in 1 ns and the rest of the system is then relaxed for 5 ns.

APPENDIX B: SWITCHING-SCHEME AND FRUSTRATED-STATE TRANSITIONS

Here we discuss the switching-scheme transition and frustrated-state transition as a function of DMI for the points indicated in Fig. 6(a). Comparing the DW width $\delta_{DW} = \pi\sqrt{A/K_{\text{eff}}}$ and the OOP nanomagnet size of 50 nm, we obtain a DW width equal to the OOP region size for $K_u = 439$ kJ/m^3. For larger K_u, the DW width is smaller than the nanomagnet size, and we observe DW switching. For smaller K_u, as in Fig. 6(b), we observe mainly coherent switching (case C), except for high DMI, where the DMI favors the tilting of the magnetic moments close to the edges (cases B and A). In Fig. 6(c), we can see that when the DMI is increased, the frustrated state gradually transitions from a frustrated NDW with only DMI energy to a frustrated TBDW (case E′ to case C′). The increasing DMI indeed leads to the tilting of the magnetic moments towards the transverse direction to decrease the DMI energy, at the expense of the other energy terms. On further increase of the DMI ($D \approx 2$ mJ/m^2), the magnetic moments near the OOP region rotate even more, to form a complete transverse DW (cases B′ and A′). In this region, the decrease of the DMI energy stabilizes the frustrated state (E_{frust} decreases), leading to the shrinking of the working window, and the deviation of the operating window from the analytical curve.

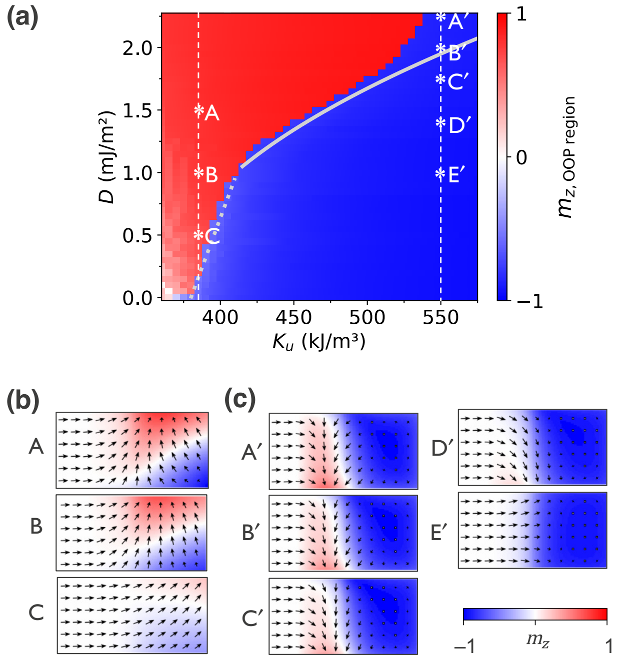

FIG. 6. (a) See Fig. 2(b): z component of the magnetization of the OOP region after imposition of the switching of the IP region, depending on DMI and K_u, for the system represented in Fig. 2(a). (b) Micromagnetic configuration (top view) of the switching mechanisms for $K_u = 385$ kJ/m^3 corresponding to points A, B, and C in (a). (c) Micromagnetic configuration (top view) of the frustrated states for $K_u = 550$ kJ/m^3 corresponding to points A', B', C', D', and E' in (a).

APPENDIX C: SWITCHING TIME

Figure 7 shows the switching time t_{sw} of the OOP region driven by chiral coupling as a function of D and K_u. As a general trend, the further we move from the boundary of the switching region, the faster the OOP region switches because the difference between E_{frust} and E_b increases.

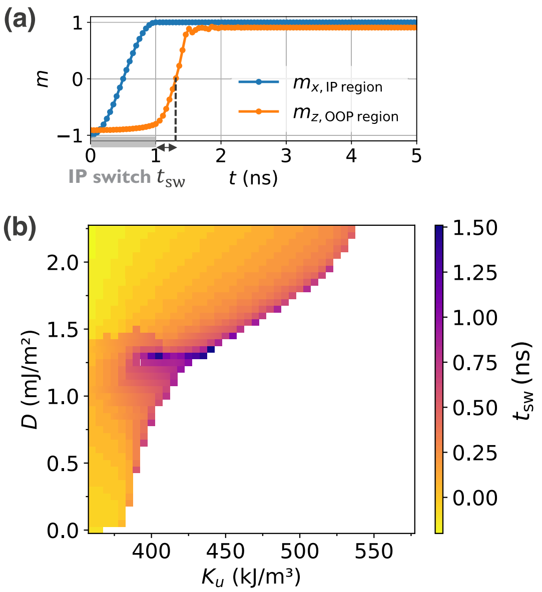

FIG. 7. (a) Example of the evolution of the magnetization of the IP and OOP regions for $K_u = 475$ kJ/m^3 and $D = 1.75$ mJ/m^2. The switching time is defined as the time needed for the OOP region to reach $m_z = 0$ after the IP region has been fully switched. (b) Switching time of the OOP region, as defined in (a), for the simulations in Fig. 2(b).

Moreover, at the transition between the two types of frustrated state (at $D \approx 1.3$ mJ/m^2), the switching time is longer.

APPENDIX D: SOT SWITCHING DYNAMICS

Here we discuss the dynamics of the IP region under SOT for the points indicated in Fig. 8(a). In Fig. 8(c) with $K_u = 375$ kJ/m^3, for increasing J_{SOT}, we first observe no switching (D), then switching by oscillations (C) and finally switching in one step (B and A). Those different behaviors are attributed to the competition of the SOT current against the chiral coupling and energy barrier of the OOP region. In Fig. 8(d) with $K_u = 550$ kJ/m^3, for increasing J_{SOT}, we first observe no switching (D′), then oscillations (C′), partial switching (B′), and finally nearly complete switching (A′) [see also Fig. 8(b)]. However in this case, since the OOP region does not switch, the IP region switches back to its initial state when the SOT is cut off at 5 ns in order to satisfy the DMI chirality.

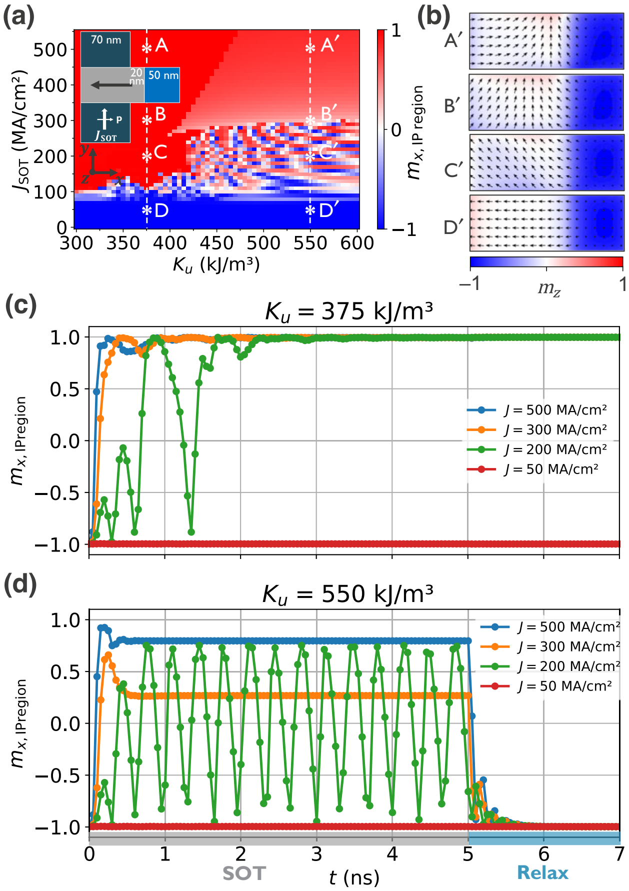

FIG. 8. (a) See Fig. 3(c): x component of the magnetization of the IP region after application of SOT on the IP region for 5 ns, depending on J_{SOT} and K_u, with $D = 1.5$ mJ/m^2. (b) Micromagnetic configurations (top view) after 5 ns of SOT corresponding to points A', B', C', and D' in (a). (c),(d) Evolution of the x component of the magnetization of the IP region when SOT is applied for 5 ns and then the system is allowed to relax for 2 ns, with (c) $K_u = 375$ kJ/m^3 and (d) $K_u = 550$ kJ/m^3 and for different values of J_{SOT} corresponding to the points indicated in (a).

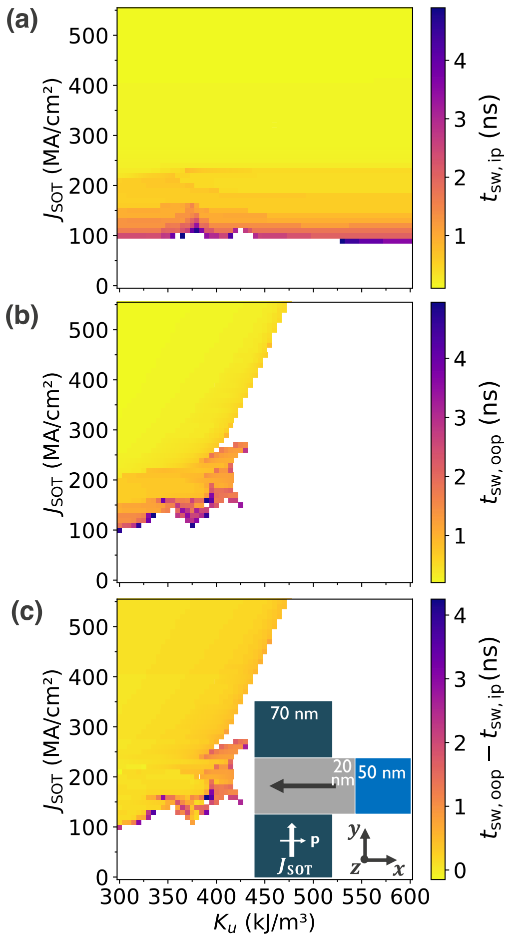

FIG. 9. (a) Switching time of the IP region, (b) switching time of the OOP region, and (c) difference $t_{\mathrm{sw,OOP\ region}} - t_{\mathrm{sw,IP\ region}}$ for the system represented in the inset, with $D = 1.5$ mJ/m^2 (corresponding to Fig. 3). The switching time is defined as the time needed to reach $m_x = 0$ for the IP region and the time needed to reach $m_z = 0$ for the OOP region.

Figure 9 shows the switching time $t_{\mathrm{sw,IP\ region}}$ of the IP region, the switching time $t_{\mathrm{sw,OOP\ region}}$ of the OOP region, and the difference $t_{\mathrm{sw,OOP\ region}} - t_{\mathrm{sw,IP\ region}}$ as a function of J_{SOT} and K_u. As expected, the switching time of the IP region decreases for increasing J_{SOT}. Moreover, the switching of the OOP region by chiral coupling follows the switching of the IP region in the nanosecond time range.

[1] I. Dzyaloshinsky, A thermodynamic theory of "weak" ferromagnetism of antiferromagnetics, J. Phys. Chem. Solids **4**, 241 (1958).

[2] T. Moriya, Anisotropic superexchange interaction and weak ferromagnetism, Phys. Rev. **120**, 91 (1960).

[3] H. Yang, J. Liang, and Q. Cui, First-principles calculations for Dzyaloshinskii–Moriya interaction, Nat. Rev. Phys. **5**, 43 (2022).

[4] T. Yu, Z. Luo, and G. E. Bauer, Chirality as generalized spin–orbit interaction in spintronics, Phys. Rep. **1009**, 1 (2023).

[5] S. Parkin and S.-H. Yang, Memory on the racetrack, Nat. Nanotechnol. **10**, 195 (2015).

[6] A. Thiaville, S. Rohart, É. Jué, V. Cros, and A. Fert, Dynamics of Dzyaloshinskii domain walls in ultrathin magnetic films, Europhys. Lett. **100**, 57002 (2012).

[7] A. Fert, N. Reyren, and V. Cros, Magnetic skyrmions: Advances in physics and potential applications, Nat. Rev. Mater. **2**, 17031 (2017).

[8] M. Kuepferling, A. Casiraghi, G. Soares, G. Durin, F. Garcia-Sanchez, L. Chen, C. Back, C. Marrows, S. Tacchi, and G. Carlotti, Measuring interfacial Dzyaloshinskii-Moriya interaction in ultrathin magnetic films, Rev. Mod. Phys. **95**, 015003 (2023).

[9] A. Fert, M. Chshiev, A. Thiaville, and H. Yang, From early theories of Dzyaloshinskii-Moriya interactions in metallic systems to today’s novel roads, J. Phys. Soc. Jpn. **92**, 081001 (2023).

[10] S.-H. Yang, R. Naaman, Y. Paltiel, and S. S. P. Parkin, Chiral spintronics, Nat. Rev. Phys. **3**, 328 (2021).

[11] M. S. N. Tey, X. Chen, A. Soumyanarayanan, and P. Ho, Chiral spin textures for next-generation memory and unconventional computing, ACS Appl. Electron. Mater. **4**, 5088 (2022).

[12] Z. Luo, T. P. Dao, A. Hrabec, J. Vijayakumar, A. Kleibert, M. Baumgartner, E. Kirk, J. Cui, T. Savchenko, G. Krishnaswamy, L. J. Heyderman, and P. Gambardella, Chirally coupled nanomagnets, Science **363**, 1435 (2019).

[13] R. A. Duine, K.-J. Lee, S. S. P. Parkin, and M. D. Stiles, Synthetic antiferromagnetic spintronics, Nat. Phys. **14**, 217 (2018).

[14] C. O. Avci, C.-H. Lambert, G. Sala, and P. Gambardella, Chiral coupling between magnetic layers with orthogonal magnetization, Phys. Rev. Lett. **127**, 167202 (2021).

[15] S. H. Skjærvø, C. H. Marrows, R. L. Stamps, and L. J. Heyderman, Advances in artificial spin ice, Nat. Rev. Phys. **2**, 13 (2019).

[16] Z. Luo, A. Hrabec, T. P. Dao, G. Sala, S. Finizio, J. Feng, S. Mayr, J. Raabe, P. Gambardella, and L. J. Heyderman, Current-driven magnetic domain-wall logic, Nature **579**, 214 (2020).

[17] D. Yu, Y. Ga, J. Liang, C. Jia, and H. Yang, Voltage-controlled Dzyaloshinskii-Moriya interaction torque switching of perpendicular magnetization, Phys. Rev. Lett. **130**, 056701 (2023).

[18] J. C. Slonczewski, Current-driven excitation of magnetic multilayers, J. Magn. Magn. Mater. **159**, L1 (1996).

[19] S. Bhatti, R. Sbiaa, A. Hirohata, H. Ohno, S. Fukami, and S. Piramanayagam, Spintronics based random access memory: A review, Mater. Today **20**, 530 (2017).

[20] I. M. Miron, K. Garello, G. Gaudin, P.-J. Zermatten, M. V. Costache, S. Auffret, S. Bandiera, B. Rodmacq, A. Schuhl, and P. Gambardella, Perpendicular switching of a single ferromagnetic layer induced by in-plane current injection, Nature **476**, 189 (2011).

[21] L. Zhu, Switching of perpendicular magnetization by spin-orbit torque, Adv. Mater. **35**, 2300853 (2023).

[22] T. Nozaki, T. Yamamoto, S. Miwa, M. Tsujikawa, M. Shirai, S. Yuasa, and Y. Suzuki, Recent progress in the voltage-controlled magnetic anisotropy effect and the challenges faced in developing voltage-torque MRAM, Micromachines **10**, 327 (2019).

[23] A. V. Kimel and M. Li, Writing magnetic memory with ultrashort light pulses, Nat. Rev. Mater. **4**, 189 (2019).

[24] J. Igarashi, W. Zhang, Q. Remy, E. Díaz, J.-X. Lin, J. Hohlfeld, M. Hehn, S. Mangin, J. Gorchon, and G. Malinowski, Optically induced ultrafast magnetization switching in ferromagnetic spin valves, Nat. Mater. **22**, 725 (2023).

[25] A. Vansteenkiste, J. Leliaert, M. Dvornik, M. Helsen, F. Garcia-Sanchez, and B. V. Waeyenberge, The design and verification of MuMax3, AIP Adv. **4**, 107133 (2014).

[26] P. Bouquin, S. Rao, G. S. Kar, and T. Devolder, Size dependence of spin-torque switching in perpendicular magnetic tunnel junctions, Appl. Phys. Lett. **113**, 222408 (2018).

[27] M. Baumgartner, K. Garello, J. Mendil, C. O. Avci, E. Grimaldi, C. Murer, J. Feng, M. Gabureac, C. Stamm, Y. Acremann, S. Finizio, S. Wintz, J. Raabe, and P. Gambardella, Spatially and time-resolved magnetization dynamics driven by spin–orbit torques, Nat. Nanotechnol. **12**, 980 (2017).

[28] M. Heide, G. Bihlmayer, and S. Blügel, Dzyaloshinskii-Moriya interaction accounting for the orientation of magnetic domains in ultrathin films: Fe/W(110), Phys. Rev. B **78**, 140403 (2008).

[29] See Supplemental Material at http://link.aps.org/supplemental/10.1103/PhysRevApplied.21.024050 for more details about the scaling potential, the potential for experimental demonstration, and the limitations of current-driven domain-wall logic, in which Refs. [8,46–49] are cited.

[30] Q. Shao, *et al.*, Roadmap of spin-orbit torques, IEEE Trans. Magn. **57**, 1 (2021).

[31] H. Wu, J. Zhang, B. Cui, S. A. Razavi, X. Che, Q. Pan, D. Wu, G. Yu, X. Han, and K. L. Wang, Field-free approaches for deterministic spin–orbit torque switching of the perpendicular magnet, Mater. Futures **1**, 022201 (2022).

[32] V. Lopez-Dominguez, Y. Shao, and P. K. Amiri, Perspectives on field-free spin–orbit torque devices for memory and computing applications, J. Appl. Phys. **133**, 040902 (2023).

[33] S. Fukami, T. Anekawa, C. Zhang, and H. Ohno, A spin–orbit torque switching scheme with collinear magnetic easy axis and current configuration, Nat. Nanotechnol. **11**, 621 (2016).

[34] H. Yoda, N. Shimomura, Y. Ohsawa, S. Shirotori, Y. Kato, T. Inokuchi, Y. Kamiguchi, B. Altansargai, Y. Saito, K. Koi, H. Sugiyama, S. Oikawa, M. Shimizu, M. Ishikawa, K. Ikegami, and A. Kurobe, in *2016 IEEE International Electron Devices Meeting (IEDM)* (IEEE, San Francisco, CA, USA, 2016), p. 27.6.1.

[35] K. Cai, S. Van Beek, S. Rao, K. Fan, M. Gupta, V. D. Nguyen, G. Jayakumar, G. Talmelli, S. Couet, and G. S. Kar, in *2022 IEEE Symposium on VLSI Technology and Circuits (VLSI Technology and Circuits)* (IEEE, Honolulu, HI, USA, 2022), p. 375.

[36] A. Du, D. Zhu, K. Cao, Z. Zhang, Z. Guo, K. Shi, D. Xiong, R. Xiao, W. Cai, J. Yin, S. Lu, C. Zhang, Y. Zhang, S. Luo, A. Fert, and W. Zhao, Electrical manipulation and detection of antiferromagnetism in magnetic tunnel junctions, Nat. Electron. **6**, 425 (2023).

[37] R. Carpenter, W. Kim, K. Sankaran, N. Ao, M. Ben Chroud, A. Kumar, A. Trovato, G. Pourtois, S. Couet, and G. S. Kar, in *2021 IEEE International Electron Devices Meeting (IEDM)* (IEEE, San Francisco, CA, USA, 2021), p. 17.6.1.

[38] Y. Shao, V. Lopez-Dominguez, N. Davila, Q. Sun, N. Kioussis, J. A. Katine, and P. K. Amiri, Sub-volt switching of nanoscale voltage-controlled perpendicular magnetic tunnel junctions, Commun. Mater. **3**, 87 (2022).

[39] R. Saha, Y. P. Pundir, and P. K. Pal, Comparative analysis of STT and SOT based MRAMs for last level caches, J. Magn. Magn. Mater. **551**, 169161 (2022).

[40] L. Zhu, D. C. Ralph, and R. A. Buhrman, Maximizing spin-orbit torque generated by the spin Hall effect of Pt, Appl. Phys. Rev. **8**, 031308 (2021).

[41] S. Van Beek, K. Cai, S. Rao, G. Jayakumar, S. Couet, N. Jossart, A. Chasin, and G. S. Kar, in *2022 IEEE International Reliability Physics Symposium (IRPS)* (IEEE, Dallas, TX, USA, 2022), p. 4A.2-1.

[42] D. E. Nikonov, G. I. Bourianoff, and T. Ghani, Proposal of a spin torque majority gate logic, IEEE Electron Device Lett. **32**, 1128 (2011).

[43] S. Das, A. Chen, and M. Marinella, in *2021 IEEE International Roadmap for Devices and Systems Outbriefs* (IEEE, Santa Clara, CA, USA, 2021).

[44] A. Vaysset, M. Manfrini, D. E. Nikonov, S. Manipatruni, I. A. Young, G. Pourtois, I. P. Radu, and A. Thean, Toward error-free scaled spin torque majority gates, AIP Adv. **6**, 065304 (2016).

[45] S. Breitkreutz, J. Kiermaier, I. Eichwald, X. Ju, G. Csaba, D. Schmitt-Landsiedel, and M. Becherer, Majority gate for nanomagnetic logic with perpendicular magnetic anisotropy, IEEE Trans. Magn. **48**, 4336 (2012).

[46] E. Raymenants, O. Bultynck, D. Wan, T. Devolder, K. Garello, L. Souriau, A. Thiam, D. Tsvetanova, Y. Canvel, D. E. Nikonov, I. A. Young, M. Heyns, B. Soree, I. Asselberghs, I. Radu, S. Couet, and V. D. Nguyen, Nanoscale domain wall devices with magnetic tunnel junction read and write, Nat. Electron. **4**, 392 (2021).

[47] S. Couet, S. Rao, S. Van Beek, V. D. Nguyen, K. Garello, V. Kateel, G. Jayakumar, J. D. Costa, K. Cai, F. Yasin, D. Crotti, and G. S. Kar, in *2021 Symposium on VLSI Technology* (IEEE, Kyoto, Japan, 2021), p. 1.

[48] C. Chappert, H. Bernas, J. Ferré, V. Kottler, J.-P. Jamet, Y. Chen, E. Cambril, T. Devolder, F. Rousseaux, V. Mathet, and H. Launois, Planar patterned magnetic media obtained by ion irradiation, Science **280**, 1919 (1998).

[49] R. Juge, K. Bairagi, K. G. Rana, J. Vogel, M. Sall, D. Mailly, V. T. Pham, Q. Zhang, N. Sisodia, M. Foerster, L. Aballe, M. Belmeguenai, Y. Roussigné, S. Auffret, L. D. Buda-Prejbeanu, G. Gaudin, D. Ravelosona, and O. Boulle, Helium ions put magnetic skyrmions on the track, Nano Lett. **21**, 2989 (2021).